Design of Ferrite Assisted Synchronous Reluctance machines robust towards demagnetization

(Article begins on next page)

17 April 2024

# Design of Ferrite Assisted Synchronous Reluctance machines robust towards demagnetization

A. Vagati, B. Boazzo, P. Guglielmi and G. Pellegrino

Politecnico di Torino, Corso Duca degli Abruzzi 24, 10129, Torino, Italy

*Abstract* – **The design of ferrite-assisted synchronous reluctance machines is investigated, with particular attention to the pivotal aspect of avoiding irreversible de-magnetization. Geometric rules for obtaining a robust design are proposed and described analytically. The safe operating area is quantified in terms of the corresponding maximum electrical loading. Such demagnetization limit shows to be depending on the operating temperature and the machine size. Furthermore, the comparison between the continuous load and de-magnetization conditions shows that low and medium size machines can be stiffer against demagnetization, with respect to larger machines, and have room for transient overload. The analysis is validated by finite-elements and a design example is given, namely a twelve poles direct-drive machine, rated 910 Nm, 200 rpm.**

*Index Terms*—**Ferrites, Synchronous motor drives, Synchronous machines, AC motor drives, Wind power generation, Permanent magnet machines.**·

## LIST OF SYMBOLS

| | |
|---|---|
| $D$ | stator outer diameter [m] |
| $r$ | rotor radius [m] |
| $l$ | stack length [m] |
| $g$ | airgap thickness [m] |
| $a$ | pole pitch at the airgap [m] |
| $p$ | number of pole pairs |
| $l_t$ | stator tooth length [m] |
| $F_q$ | peak of the fundamental $q$-axis mmf [A-turn] |
| $A_{q,irr}$ | $q$-electric loading leading to demagnetization [A-turn/m] |
| $A_{th}$ | electric loading at continuous operation [A-turn/m] |
| $n_r$ | number of equivalent rotor slots per pole-pair |
| $\Delta\xi_r$ | rotor slot pitch, [elt. radians] |
| $n$ | number of rotor layers |
| $k$ | index for $n$-dimensional variables |
| $S_k$ | half-width of the $k$-th flux barrier [m] |
| $l_k$ | thickness of the $k$-th flux barrier [m] |
| $l_a$ | total insulation, sum of all $l_k$ [m] |
| $l_{a,pu}$ | total insulation, in per-unit of $a/2$ |
| $p_{b,k}$ | p.u. permeance of half flux barrier |
| $p_g$ | p.u. airgap permeance of one rotor tooth |
| $f_{q,k}$ | p.u. $k$-th step of the stator mmf distribution |
| $f_{qn}$ | top level of the p.u. stator mmf, for the case of $n$ layers |
| $m_{,k}$ | p.u. mmf generated by the $k$-th barrier's magnet |
| $r_{,k}$ | p.u. magnetic potential of the $k$-th rotor segment |
| $\phi_k$ | p.u. flux through half the $k$-th rotor barrier |
| $B_{m,k}$ | flux density in the $k$-th magnet [T] |
| $B_{m0}$ | flux density in the magnets at no-load [T] |
| $B_{m,irr}$ | lower limit of reversible demagnetization [T] |
| $B_r$ | PM remanence [T] |

## I. INTRODUCTION

Permanent Magnet (PM) machines are appreciated and widely adopted for their high torque density and efficiency. Both surface-mounted PM (SPM) and interior PM (IPM) rotor types are used, depending on the application [1,2]. Most of up to date PM synchronous machines are based on rare-earth magnetic materials, namely NdFeB grades, because of their large remanence and coercivity values.

Recently, the volatility of Nd-magnets price has compelled the designers and manufacturers of electrical machines to find alternative solutions, especially in those applications where the quantity of PM material is significant (e.g. large direct drive machines) or impacts the industrial cost, like in mass production (e.g. automotive, home appliances, etc.).

In this perspective, the mere substitution of surface mounted Nd-magnets with low cost hard ferrite pieces would not produce a comparable performance. For example, a SPM motor with ferrite magnets would have a much lower airgap flux density [4] and then torque. In IPM rotors the flux of ferrite magnets can be concentrated to increase the airgap flux density, but still they can hardly match the torque density values of Nd based counterparts [5-6].

A different way of using the PMs in synchronous motor drives is to PM-assist a multiple barriers Synchronous Reluctance (SR) machine. In this case the role of the PMs is more to adjust the power factor of the SR machine, rather than to produce torque directly. PM-assisted SR machines have a torque density that is comparable with the one of other PM machines [1-3,7] with a limited quantity of Nd magnets inserted into the flux barriers [8]. Alternatively, the rotor flux barriers can be filled with a greater quantity of a weaker magnetic material, such as hard ferrite, still obtaining a competitive performance [9-10].
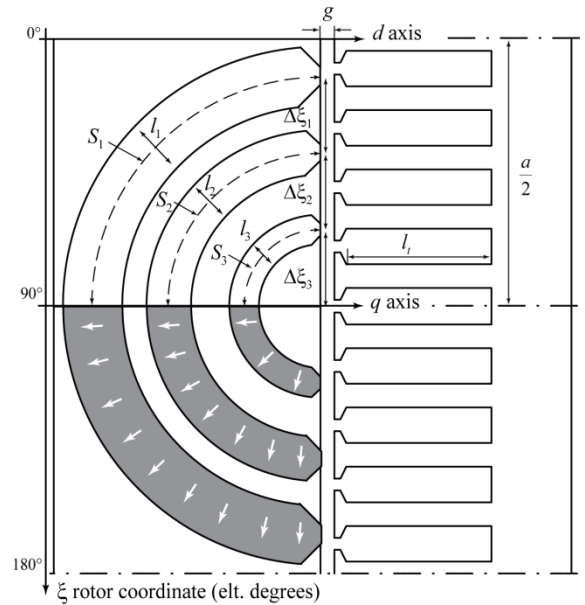


Fig. 1. Reference geometry of the example three layers rotor. The barriers widths $S_{123}$ are referred to one half pole. The PMs are magnetized radial-wise, against the $q$ axis, according to the defined $dq$ axes.

Ferrite-assisted Synchronous Reluctance (FASR) machines can even reach the performance of a Nd-assisted

counterpart, but they are known for being fragile towards de-magnetization, in particular when very low temperatures are considered. Some recent papers have put in evidence that the electric loading must be limited, and the flux barriers must be shaped properly to avoid de-magnetization [11-12]. Yet, no systematic approach has been proposed for the design of FASR machines, and for quantifying their stiffness towards de-magnetization as a function of size and loading.

The paper addresses how to design the rotor barriers in order to exploit the ferrite uniformly and increase the robustness against de-magnetization. Analytical relationships are developed with reference to the fundamental geometry of one rectified pole reported in Fig. 1. The flux barriers have constant thickness ($l_k$, with $k = 1,2,3$) along the respective widths ($S_k$) and are completely filled with ferrite, to compensate for the lower energy density of the low cost magnet with a larger volume of material.

After the section dedicated to the barriers geometry, the electric loading limit corresponding to de-magnetization is expressed in equations, and then compared to the one corresponding to continuous operation. Last, one machine example is designed and finite element validated, referring to a small size direct drive wind turbine generator.

## II. GENERAL ASSUMPTIONS AND FASR MODEL

### A. Reference geometry

The reference geometry in Fig. 1 represents a rectified FASR machine with distributed windings. At first, round shaped barriers are considered, eventually replaced by more compact shapes in the final design. The $dq$ axes are defined according to the synchronous reluctance style, being this basically a SR machine, although PM-assisted. The number of layers is indicated with $n$ and reference will be made to $n = 3$ as an example, but the key formulas have general validity. The key-geometric parameters indicated in Fig.1 are: the airgap length ($g$), the pole pitch ($a$), the stator teeth length ($l_t$), the pitch of the $k$-th rotor "slot" ($\Delta\xi_k$), half the width of the $k$-th layer ($S_k$) and its thickness ($l_k$), that is uniform over the whole barrier span.

### B. General design assumptions

The first key design choice is that the barriers must have constant thickness. This comes from having the layers full of ferrite: a non constant thickness would cause non-uniform values of flux density, and the occurrence of weaker points more prone to demagnetization in the thinner sections of each layer, like for example the extremities [11].

Another key choice here is the regular rotor pitch, related to torque ripple minimization [13]. The number of equivalent rotor slots per pole pair, called $n_r$, and the rotor pitch $\Delta\xi_r$ are related by (1), in electrical radians.

$$\Delta\xi_{r,k} = \frac{2\pi}{n_r} \qquad k = 1,2,3 \qquad (1)$$

Choices other than (1) are possible, but most of the literature agrees that a regular or quasi-regular rotor pitch, properly chosen [13-20], keeps the torque ripple low. The choice of $n_r$ is related to the number of slots per pole-pair of the stator [13,15]. The $n$-th rotor pitch, the one across the $q$-axis ($\Delta\xi_3$ in Fig. 1), is again equal to $\Delta\xi_r$ in Fig. 1, according

to what is called a "complete" rotor in [13]. When $\Delta\xi_n > \Delta\xi_r$, the rotor structure is called "incomplete", instead. In the following, reference will be made to complete structures. All the formulas can be complicated to include incomplete machines with formal modifications that do not change the conclusions of the paper.

### C. Model accuracy at lower pole pair numbers

The rectified geometry of Fig. 1 is very similar to the actual pole of a rotating machine with a high number of poles, as it is the case for low speed, direct-drive applications. For low pole pair numbers, the model is less accurate because the pole curvature reduces the barriers widths $S_{123}$ with respect to Fig. 1, where they are $\pi/2$ times larger than the respective airgap chord. The smaller barrier widths produce more insulation along the $q$ axis than the one predicted by the model. Therefore, the model in Fig. 1 is accurate for high pole numbers and progressively tends to be conservative when applied to lower pole numbers, in terms of machine saliency (i.e. torque) and insulation (i.e. stiffness against de-magnetization).

### D. Circuital model of the q-axis

The circuit reported in Fig. 2 represents the $q$-axis magnetic model of the 3-layer example. The fluxes are the ones of half a pole. The magneto-motive force (mmf) generators indicated with $f_{q123}$ stand for the stator mmf staircase in Fig. 3, the $m_{123}$ generators, along with the respective barrier permeances $p_{b123}$, represent the barriers filled with permanent magnets. The terms $p_g$ are the permeances of the rotor teeth at the airgap. They are all equal, due to the regular rotor pitch. The magnetic potentials $r_{123}$ represent the rotor iron segments, assumed to be equipotential (no gradient of mmf along the steel flux guides).
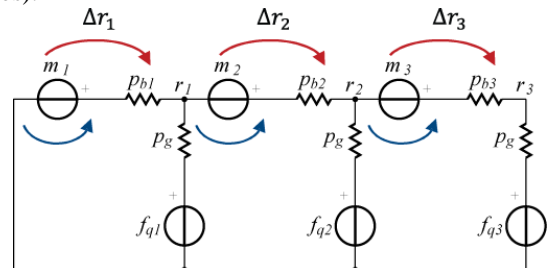
Fig. 2. Equivalent circuit of the three layer rotor machine when a $q$-axis mmf distribution $[f_{q1}, f_{q2}, f_{q3}]$ is applied against the PMs.
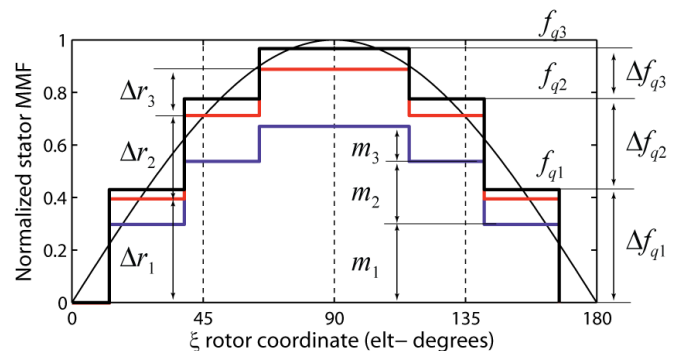
Fig. 3. Per-unit stator mmf distribution, produced by a sinusoidal mmf wave aligned with the rotor $q$ axis.

The mmf staircase $f_{q123}$ comes from the discretization of the fundamental mmf produced by the stator windings, as illustrated in Fig. 3. The sinusoidal mmf is averaged across

each rotor steel segment at the airgap. Fig. 3 accounts for the effect of the *q*-axis current component only, that is the one aligned against the PMs, as defined in Fig. 1.

The rotor in Fig. 1 has no connection bridges between the steel pieces, and neither such structural ribs have been included in the magnetic equivalent circuit of Fig. 2. Their effect must be necessarily taken into account when dealing with the evaluation of torque and power factor, like in [13,20]. However, the focus of this paper is demagnetization, and ribs have a negligible impact in this sense. At zero current they to load the PMs further, but this is not a dangerous operating point. When a de-magnetizing current is applied against the magnets, the ribs shunt a portion of the flux crossing the barriers and release the PMs of a (small) part of their loading. This is why it is not critical to assume that there are no ribs in the circuit, as also confirmed by Finite Element Analysis (FEA) at section V.

### E.    *Normalization of the model*

The mmf generators, magnetic potentials and permeances in Fig. 2 are expressed in normalized quantities. The base value used for all mmfs is the peak of the fundamental *q*-axis mmf (2):

$$F_q = \frac{3}{\pi} \cdot k_w \cdot \frac{N}{p} \cdot I_q \qquad (2)$$

Where $I_q$ is the *q*-axis current component, $k_w$ is the winding factor, $N$ is the number of turns in series per phase, $p$ is the number of pole pairs. The normalized mmf generators, corresponding to the remanence of the ferrite magnets and to their thicknesses, are expressed as:

$$m_k = \frac{\frac{B_r}{\mu_0} l_k}{F_q} \quad k = 1,2,3 \qquad (3)$$

with $B_r$ being the remanence of the permanent magnets. Fig. 3 shows that the per-unit fundamental stator mmf has a unitary amplitude, after it is normalized by $F_q$. This to say that the mmf base quantity can vary with the actual current loading applied to the machine.

The permeances are normalized such that they are simply the ratio between the width and the length of the respective flux tube. For example, the normalized permeance of the *k*-th half barrier is:

$$p_{b,k} = \frac{S_k}{l_k} \quad k = 1,2,3 \qquad (4)$$

The base value of permeances is $\mu_0 \cdot l$, being $l$ the stack length and $\mu_0$ the permeability of free space. The normalized permeance of all flux tubes at the airgap is:

$$p_g = \frac{1}{k_c} \cdot \frac{a}{g} \cdot \frac{\Delta \xi_r}{\pi} \qquad (5)$$

Where $k_c$ is the Carter coefficient. The very simple formulations of (4) and (5) come from the constant thickness and the constant rotor pitch assumptions, respectively.

Last, the base quantity for per-unit fluxes follows the previous ones, and it is $\mu_0 \cdot l\, F_q$.

### F.    *Solution of the q-axis magnetic circuit*

The circuit of Fig. 2 is expressed by the system of linear equations (6):

$$A \cdot \Delta r = B \cdot m + C \cdot \Delta f_q \qquad (6)$$

Where the magnetic potentials are expressed in form of vectors of three elements:

$$\Delta r = \begin{bmatrix} \Delta r_1 \\ \Delta r_2 \\ \Delta r_3 \end{bmatrix} = \begin{bmatrix} r_1 \\ r_2 - r_1 \\ r_3 - r_2 \end{bmatrix} \qquad (7)$$

$$m = \begin{bmatrix} m_1 \\ m_2 \\ m_3 \end{bmatrix} \qquad (8)$$

$$\Delta f_q = \begin{bmatrix} \Delta f_{q1} \\ \Delta f_{q2} \\ \Delta f_{q3} \end{bmatrix} = \begin{bmatrix} f_{q1} \\ f_{q2} - f_{q1} \\ f_{q3} - f_{q2} \end{bmatrix} \qquad (9)$$

The matrices $A$, $B$ and $C$ in (6) have the expressions given in (10)-(12) that are a function of the barriers geometries (through the permeances $p_{b123}$), given the permeances of the airgap flux tubes, all equal to $p_g$.

$$A = \begin{bmatrix} \frac{p_{b1}}{p_g}+1 & -\frac{p_{b2}}{p_g} & 0 \\ 1 & \frac{p_{b2}}{p_g}+1 & -\frac{p_{b3}}{p_g} \\ 1 & 1 & \frac{p_{b3}}{p_g}+1 \end{bmatrix} \qquad (10)$$

$$B = \begin{bmatrix} \frac{p_{b1}}{p_g} & -\frac{p_{b2}}{p_g} & 0 \\ 0 & \frac{p_{b2}}{p_g} & -\frac{p_{b3}}{p_g} \\ 0 & 0 & \frac{p_{b3}}{p_g} \end{bmatrix} \qquad (11)$$

$$C = \begin{bmatrix} 1 & 0 & 0 \\ 1 & 1 & 0 \\ 1 & 1 & 1 \end{bmatrix} \qquad (12)$$

The solution of (6), in terms of rotor potentials, is:

$$\Delta r = (A^{-1}B) \cdot m + (A^{-1}C) \cdot \Delta f_q \qquad (13)$$

### G.    *Flux density in the permanent magnets*

From the equivalent circuit, the flux through half the *k*-th magnet, in per-unit, is:

$$\phi_{m,k} = (m_k - \Delta r_k) \cdot p_{bk} \qquad (14)$$

The flux density in the magnet, measured in Tesla, is given by (15), where the per-unit flux has been de-normalized per $\mu_0 \cdot F_q \cdot l$ .

$$B_{m,k} = \frac{\phi_{m,k} \cdot \mu_o \cdot l\, F_q}{l \cdot S_k} = \frac{(m_k - \Delta r_k) \cdot p_{bk}}{S_k} \cdot \mu_o \cdot F_q \quad (15)$$

By manipulation of (15), (3) and (4), the PM flux density of each magnet, divided by the PM remanence $B_r$, is:

$$\frac{B_{m,k}}{B_r} = 1 - \frac{\Delta r_k}{m_k} < \frac{B_{m,irr}}{B_r} \qquad (16)$$

Each magnet is safe from demagnetization if its flux density is above the limit of irreversible de-magnetization $B_{m,irr}$, as defined in (16). This depends on the PM grade and the operating temperature.

## H. Design of the flux barriers

Provided that the ratio $\Delta r_k/m_k$ in (16) determines the flux density of the $k$-th magnet, the vector equation (13) is reorganized as follows:

$$\frac{\Delta r}{m} = (A^{-1}B) + (A^{-1}C) \cdot \frac{\Delta f_q}{m} \qquad (17)$$

where the vector-divide symbol indicates the element by element division between vectors. If the flux barriers are designed so to make the $\Delta r$ and $m$ vectors proportional according to a scalar factor, as indicated in (18), then the PMs of all layers work at the same flux density, and (16) becomes (19).

$$\frac{\Delta r}{m} = f(I_q) \cdot I \qquad (18)$$

$$\frac{B_m}{B_r} = 1 - f(I_q) = f'(I_q) \qquad (19)$$

The term $I$ in (18) is the unit matrix. The $I_q$ current in (18-19) reminds that the layers magnetic potentials and the PM flux density are functions of the $q$-current loading. One straightforward way to obtain the scalar condition (18-19) is:
1)  To design the staircase $m$ to copy the shape of the staircase $\Delta f_q$, as indicated in Fig. 3, so that the result of their vector-division is a scalar coefficient, variable with the $q$ current loading. ***This first constraint determines barriers thicknesses*** (subsection II.I)**.**
2)  To design the barriers permeances such that the matrix products $A^{-1}B$ and $A^{-1}C$ in (17) are constant, scalar coefficients. ***This second constraint determines the barriers widths*** (subsection II.L)**.**

## I. Thickness of the flux barriers

According to the above point 1), the staircase $m$ must copy the shape of $\Delta f_q$, otherwise said the element by element ratio division of the two vectors gives always the same result:

$$\frac{m_k}{\Delta f_{qk}} = const \quad k = 1,2,3 \qquad (20)$$

Remembering that $m_k$ comes from the barrier thickness according to (3), it turns out that it is the thickness distribution $l_{123}$ that must once more copy the $\Delta f_{q123}$ distribution.

$$\frac{l_k}{\Delta f_{qk}} = const = \frac{\sum l_k}{\sum \Delta f_{qk}} = \frac{l_a}{f_{qn}} \qquad (21)$$

Where $l_a$ is the total insulation, sum of the barriers thicknesses and $f_{qn}$ is the top of the stator mmf staircase, that is also the sum of the elements of $\Delta f_q$. For three layers, $f_{q3} = 0.967$ (Fig. 3), and $f_{qn}$ is close to one also for any number of layers. From (21), the condition (22) is found:

$$l_k = l_a \cdot \frac{\Delta f_{qk}}{f_{qn}} \qquad (22)$$

***Given the total insulation $l_a$, this must be subdivided between the layers according to the stator mmf staircase per-unit levels.***

## J. Width of the flux barriers

As said at point 2) of subsection II.H, the two matrix products $A^{-1}B$ and $A^{-1}C$ ought to be scalar numbers. This is true, for example, when all the barrier permeances $p_{b123}$, defined in (4), are made the same:

$$p_{bk} = \frac{S_k}{l_k} = const \qquad k = 1,2,3 \qquad (23)$$

Otherwise written:

$$S_k = S_1 \frac{l_k}{l_1} \qquad k = 1,2,3 \qquad (24)$$

Where $S_1$ and $l_1$ are the dimensions of the largest barrier (Fig. 1). If the barriers thicknesses respect the condition (22), then ***also their widths $S_k$ must be proportional to the steps of the stator mmf staircase.***

To summarize, if the rotor barriers are designed according to (22) and (24), then all the mmf staircases $\Delta f_q$, $m$, $\Delta r$ have the same shape as indicated in Fig. 3 and all the PMs work at the same flux density. As said in the beginning, the flux density is also homogeneous over each magnet width due to the constant thickness of the barriers. There are neither weaker magnets nor weaker points, locally in the barriers.

## III. FEASIBLE CURRENT LOADING

Once the rotor of the FASR machine is designed in the respect of all the aforementioned rules, equation (19) is valid. From (19) the PM working point can be evaluated at all $I_q$ load conditions, and in particular at the limit of irreversible de-magnetization. As said in (16), the PM flux density must stay above the demagnetization limit $B_{m,irr}$ at all $I_q$ values, including operation and fault conditions.

The demagnetization curves in Fig. 4 show that at low temperatures hard ferrites de-magnetize irreversibly at very early values of flux density. For example, at -60°C, the safe area is $B_m > 0.27$ T, being $B_r = 0.45$ T (0.6 p.u. of remanence), while at 20°C it is $B_m > 0.1$ T, with $B_r = 0.38$ T (0.26 p.u.). The p.u. extent of the PM dangerous area is indicated with colored bars in the figure, and called $B_{m,irr,pu}$. For this ferrite grade all positive values of flux density are safe from +60°C on.
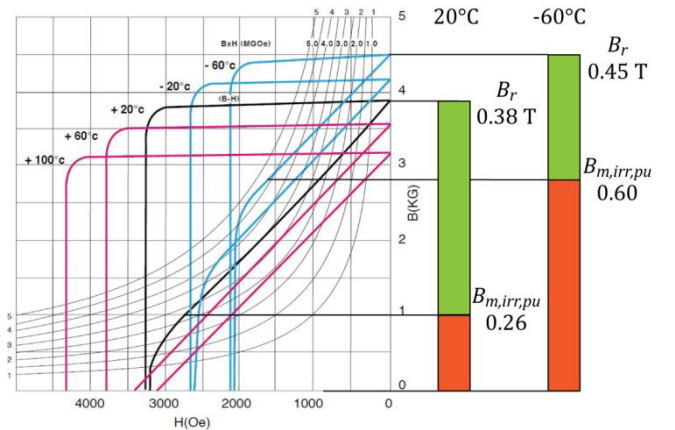


Fig. 4    B-H characteristics of the considered ferrite grade, USF by CALAMIT. The effect of temperature over the remanence and the per-unit limit of demagnetization are put in evidence.

In the following subsections, the per-unit flux density

(19) is evaluated at no load and put in relationship with the rotor geometry. Then, given the geometry, the maximum electric loading corresponding to the irreversible demagnetization condition is quantified analytically.

*A.      No load condition*

The solution of (17) with $\Delta f_q/m$ equal to zero gives $\Delta r/m$ at no load. Substituting this into (19), the PM flux density at no load (25) is found, as a function of the key geometric parameters:

$$\frac{B_{m0}}{B_r} = B_{m0,pu} = \frac{1}{1 + \frac{S_1}{l_a}\frac{g}{a}\frac{2\pi}{\Delta\xi_r}\sin\left(\frac{\Delta\xi_r}{2}\right)} \quad (25)$$

When half the rotor pitch (1) is a small angle, that is the case for the $n_r$ values corresponding to three or more barriers (Fig. 1 refers to $n_r = 14$), the term $sin(\Delta\xi_r/2)/\Delta\xi_r$ is approximately 1/2. Therefore, equation (25) becomes:

$$B_{m0,pu} \cong \frac{1}{1 + \pi\frac{S_1}{l_a}\frac{g}{a}} \quad (26)$$

With round barriers as in Fig. 1, the first barrier width is:

$$S_1 = \left(\frac{n_r - 2}{4}\right)\Delta\xi_r\frac{a}{2} = \frac{\pi}{4}a\left(1 - \frac{2}{n_r}\right) \quad (27)$$

By substituting (27) into (26), and disregarding the term $2/n_r$ (= 2/14 in the example) in $S_1$, equation (28) is found.

$$B_{m0,pu} \cong \frac{1}{1 + \frac{\pi^2}{2}\cdot\frac{1}{l_{a,pu}}\cdot\frac{g}{a}} \quad (28)$$

where the p.u. magnetic insulation $l_{a,pu} = l_a/(a/2)$ has been introduced. A high $a/g$ (i.e. a small per-unit airgap) and a high per-unit insulation keep the no-load flux density close to one per-unit (the PMs are close to their remanence value), meaning that the magnets are not heavily loaded, at least at zero current. The rotor pitch or, otherwise said, the number of layers does not appear in (28), and this approximation is true for three or more layers.

In Fig. 5, the $B_{m0,pu}$ characteristics (28) are reported as a function of the pole pitch to airgap factor $a/g$, for two different values of insulation. The two demagnetization limits indicated in the figure are the ones just calculated from Fig. 4.

According to the plots, demagnetization never occurs at 20°C, while at -60°C it is recommendable to have a good insulation and a ratio $a/g$ around 40 or more. Having a low $a/g$ ratio means that the airgap is thick with respect to the pole pitch, and the PMs are loaded significantly already in no-load conditions. Provided that the airgap size and the rotor diameter are strictly related due to mechanical costraints [21], the lower limitation to $a/g$ constitutes an upper limit to the number of poles of a rotating machine. In other words, if the airgap cannot be made smaller for a certain rotor size, the ratio $a/g$ can be increased through the choice of the number of poles: more poles means a smaller pitch $a$, given the rotor diameter, and vice-versa.

It can be concluded that *if the airgap is small enough or, vice versa, the pole pitch is large enough, there is little or no risk of demagnetization at no load*, even at arctic temperatures such as -60°C. Nevertheless, it is mandatory that a significant margin at no-load exists: in fact, $B_{m0,pu}$ *is a figure of merit of the robustness of the design of the machine also at load,* as explained in the next subsection.
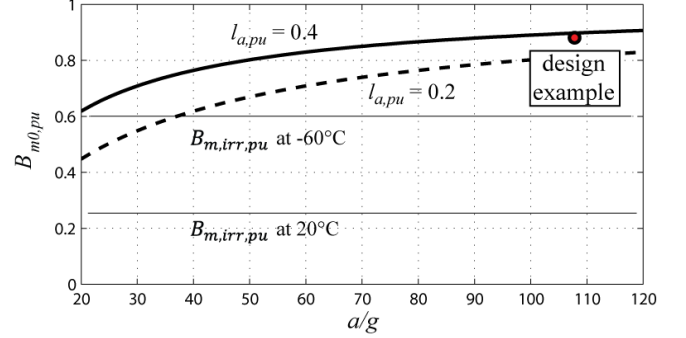


Fig. 5      No load p.u. flux density in the magnets for different values of p.u. insulation. The demagnetization limits at -60°C and 20°C are indicated.

*B.      Maximum load before demagnetization*

The aim of this paragraph is to quantify the level of current loading that leads to irreversible demagnetization, given the operating temperature. The $q$- electric loading, expressed in Aturn/m, is defined:

$$A_q = \frac{\pi}{2}\cdot\frac{F_q}{a} \quad (29)$$

Once again, it is the $q$-axis loading (against the PMs) the one of interest for de-magnetization. The relationship between the $q$-current loading and the irreversible demagnetization area $B_{m,irr,pu}$ comes by manipulation of (19), this time with $F_q \neq 0$. From (2)-(13), (19), (22) and (24) it is obtained:

$$A_{q,irr} = \frac{\pi}{4}\frac{B_r l_{a,pu}}{\mu_0 f_{qn}}\left(1 - \frac{B_{m,irr,pu}}{B_{m0,pu}}\right) \quad (30)$$

This is the key equation of the paper, indicating the electrical loading that can be tolerated by the magnets. This is proportional to the PMs remanence and to the per-unit insulation $l_{a,pu}$, as it can be intuitive. The factor $f_{qn}$ is close to one, as said after equation (21). The term in brackets says that $A_{q,irr}$ *is a function of the margin between the material property* $B_{m,irr,pu}$ *and the no load flux-density* $B_{m0,pu}$. If $B_{m0,pu}$ is too close to $B_{m,irr,pu}$, then the feasible loading tends to zero, and the feasible torque goes to zero along with. In practice, $B_{m0,pu}$ in (30) summarizes the geometry, while $B_r$ and $B_{m,irr,pu}$ summarize the combination of PM grade and operating temperature.

*C.      Effects of total insulation and temperature*

Fig. 6 reports the applicable current loading (30) as a function of the $a/g$ ratio, the insulation and the temperature. $A_{q,irr}$ grows very quickly as the PM temperature passes from -60°C to more realistic temperatures such as 20°C or more. Nevertheless, it is still possible to have good values of electric loading like 30 kA/m or more also with the PMs at -60°C, provided that both the insulation and the pitch to airgap ratio $a/g$ are high.

The example design at section V is also indicated in Fig. 6 by two red circles. The machine has $a/g = 106$ and $l_{a,pu} = 0.375$ and a no-load, $B_{m0,pu} = 0.89$, from (28). At 20°C $B_r$ is

0.38 T and $B_{m,irr,pu}$ is 0.26, from the datasheet, producing an $A_{q,irr}$ of 65.2 kA/m, calculated with (30). At -60°C the safe loading is much lower, due to the higher $B_{m,irr,pu}$ = 0.60 (with $B_r$ = 0.45 T). The applicable loading is $A_{q,irr}$ = 35.5 kA/m.

It is then of key importance that the minimum temperature specified for transient overload operation is declared accurately, because wrong specifications can compromise the feasibility of the FASR machine for the application.
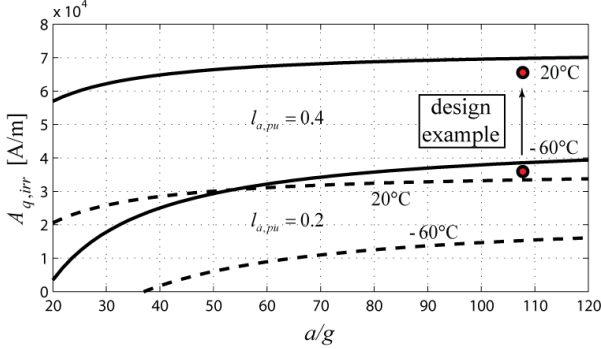


Fig. 6    Maximum electric loading as a function of the pole pitch to airgap ratio: dashed lines refer to $l_{a,pu}$ =0.2 and continuous lines to $l_{a,pu}$ =0.4. The effect of operating temperature is also shown.

Although many applications require to operate at ambient temperatures under 0°C (e.g. automotive, military, wind generation), yet it is thinkable that a temporary de-rating can be accepted when arctic temperatures such as -20°C or -60°C are considered, meaning a warm-up stage at reduced current or even a pre-heating before operation.

Going back to Fig. 6, $a/g$ values below 60 penalize the machine, as it was also evidenced at no load. The effect of $l_{a,pu}$ is more relevant on $A_{q,irr}$ than it was on $B_{m0,pu}$ in Fig. 5. This is because $l_{a,pu}$ counts twice in (30), explicitly in the formula and also implicitly through the term $B_{m0,pu}$ (28). A weak insulation, besides penalizing the reluctance torque of the machine, makes it also more prone to demagnetization and more sensitive to the pole pitch to airgap factor.

It is interesting to notice that the machines with more insulation (0.4) and a proper pole pitch ($a/g > 60$) have a resistance to demagnetization at -60°C that is comparable to the one of machines with weak insulation (0.2) at 20°C. This to say of the importance of maximizing the insulation. Last, with 20°C or more and sufficient insulation the electric loading can be very high (80 – 90 kA/m), and the resulting torque density becomes competitive with the ones obtainable with Nd-magnets excited machines. This point is addressed at subsection IV.B.

D.    *Discussion of demagnetization*

To summarize, it is possible to design a FASR machine immune from demagnetization, provided that:
- the barriers have uniform thickness.
- The barriers thicknesses and widths follow the shape of the mmf staircase, as in (22) and (24), respectively.
- the total insulation is maximized, considering that real life machines can have a per-unit insulation up to 0.35–0.40.
- the airgap and the pole pitch are matched correctly. In other words, the number of pole pairs is chosen properly, given the airgap, or vice-versa.
- High current loads are temporarily avoided when

operating at extremely low ambient temperatures.

IV.    THERMAL LIMIT AND EFFECT OF THE MACHINE SIZE

Given the type of cooling, the continuous current loading of the machine can be calculated. A quick figure of merit of the cooling properties is the power dissipation rate at the outer stack surface:

$$k_j = \frac{P_{Joule}}{\pi \cdot D \cdot l} \qquad (31)$$

$P_{joule}$ are the copper losses. Iron loss is disregarded and $D$ and $l$ are respectively the outer diameter and the length of the stator stack. The electric loading (32), corresponding to a given $k_j$, is derived, assuming a sinusoidal current waveform:

$$A_{th} = \frac{k_w}{2} \sqrt{\frac{k_j k_{cu}}{k_{end} \rho_{cu}}} \sqrt{l_t} \qquad (32)$$

$k_{cu}$ is the slot fill in factor, $k_{end}$ is the total length of the conductors (including end connections) divided by the active length, $\rho_{cu}$ is the copper resistivity, $l_t$ is the tooth length defined in Fig. 1. A fifty-fifty split between slot and tooth widths has been supposed, for simplicity.

A.    *Continuous loading and overload capability*

The comparison of the demagnetization limit (30) and the thermal limit (32) gives evidence of how irreversible demagnetization can limit the continuous and transient overload torque of FASR machines. Theoretically speaking, the two current loading values cannot be compared directly, because (30) refers to the $q$ current component only, while (32) to the whole current, included the $d$-axis component. However, de-magnetization occurs at high loads, where the current vector is close to the $q$ axis, and then assuming that (30) refers to the whole current amplitude would represent a conservative estimation of the machine current limit, for the sake of comparison with the continuous current level (32). In the following, these two limits will be compared assuming that both refer to the whole current amplitude. The actual current phase angle in maximum torque per Ampere operation will be taken into account in section V, dedicated to the design example.

In Fig.7 the continuous electric loading (32) is reported as a function of the tooth length in the two cases of $k_j$ = 3500 and 10000 W/m². The demagnetization limits (30) at -60°C and +20°C are also reported, again referring to the geometry of the machine example of section V, as in section III.C. The following parameters have been used to calculated the continuous loading in Fig.7: $k_{cu}$= 0.4, $k_{end}$ =1.5, $\rho_{cu}$=25·10⁻⁹ Ω/m (copper at 130°C) and $k_w$=0.92. The lower $k_j$ = 3500 W/m² is representative of natural ventilation, while $k_j$ = 10000 W/m² stands for forced ventilation.

Whereas $A_{q,irr}$ (30) is a function of normalized quantities only, the thermal limit $A_{th}$ (32) depends on the square root of the actual length of stator teeth, and it is then related to the physical size of the machine, meaning that larger machines can withstand a lower current density, as known.

In Fig. 7, where the rated loading (32) is lower than (30) it means that the machine can withstand transient overload at that temperature, without irreversible demagnetization. With natural ventilation ($k_j$ = 3500 W/m²) there is room for

overload even when at -60°C with teeth up to 100 mm long. This to say that *FASR machines with natural ventilation would not suffer from demagnetization at any temperature, at least in the small and medium sizes*.

With forced ventilation ($k_j$ = 10000 W/m²) the room for overload is smaller, in general. Machines with teeth 40 mm long or more are at risk of demagnetization at -60°C, in this example. This to say that *ventilated or liquid cooled machines are more at risk of demagnetization at very low temperatures, because they are more loaded*. Yet, they soon have an abundant overload margin as the operating temperature reaches reasonable values such as 20°C. The overload margin of the design example at -60°C is indicated with an arrow in Fig. 7.

Last, those machines where the continuous loading limit is higher than the demagnetization limit in Fig. 7 *may need to be warmed up at reduced load, before full load and overload can be applied.*
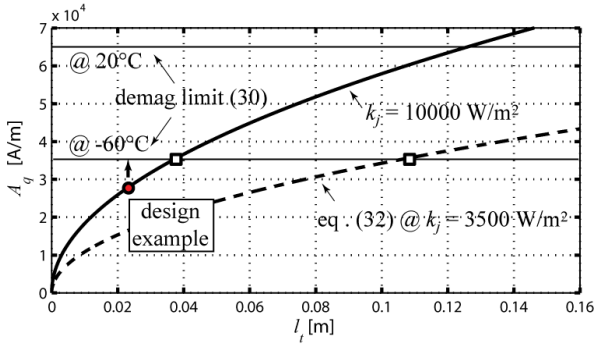


Fig. 7    Continuous electric loading versus tooth length, evaluated at 130°C (copper), for two types of cooling having $k_j$=3500W/m² and $k_j$ =10000W/m². The demagnetization levels at-60°C and 20°C (magnet) indicate the transient overload limit.

### B.    Continuous and overload torque densities

As said in subsection III.D, demagnetization tends to limit the electric loading when at very low temperatures, or in case of a bad design (high *g/a* or poor insulation). Otherwise, the applicable loading is sufficient to obtain competitive shear stress and torque density values, comparable to the ones obtainable with rare-earth SPM machines, for most of applications [22]. To account for this, the shear stress and the torque per rotor volume density of the machine example reported at section V are anticipated here. It is a wind turbine generator, rated 910 Nm at 200 rpm, specified in Tables I and II. The tree values of electric loading considered in Table I refer to continuous operation and the demagnetization limit at -60°C and 20°C, respectively, and are model-calculated. The torque and the shear stress, instead, are FEA evaluated at the maximum torque per Ampere current phase angle, at the respective current amplitudes. The shear stress is derived from the torque:

$$\sigma = \frac{T}{2\pi \cdot r^2 \cdot l} \qquad (33)$$

where *r* is the rotor radius. The magnetic loading factor (34) accounts also for the phase displacement of the magnetic and electric waves at the airgap, and it is obtained by division of the shear stress per the electric loading:

$$B \cdot cos\varphi = \frac{\sigma}{A} \qquad (34)$$

The *cos*φ factor in (34) is the machine power factor, having neglected the resistive voltage drop.

TABLE I – TORQUE DENSITY OF THE EXAMPLE FASR MACHINE, EVALUATED BY FEA

| | | Continuous operation (eq. 32) | $A = A_{q,irr}$ (eq. 30) | |
|---|---|---|---|---|
| PM temperature | [°C] | | - 60 | 20 |
| A | [kA/m] | 27.2 | 35.5 | 65.2 |
| A | % | 100 % | 130 % | 239 % |
| B cosφ | [T] | 0.82 | 0.85 | 0.88 |
| σ | [kN/m²] | 22.3 | 30.3 | 57.3 |
| σ | % | 100 % | 136 % | 257 % |
| torque/ rotor volume | [kNm/m³] | 44 | 61 | 115 |

The values in Table I say that the FASR motor can have a good torque density at continuous operation, competitive for the application. Moreover, the safe current overload is 130% already at -60°C, reaching 240% at 20°C and so on. Still, the overload figures here are under the conservative assumption that it is actually the current amplitude to be limited to (30), and not the *q*-component only. The overload situations in Table I have then a further safety margin, given the non negligible *d* current component.

The shear stress is FEA calculated with the PMs at 130°C, that is the rated temperature at continuous operation. Although the power factor, torque and shear stress may change slightly with the temperature, yet the conclusions about feasible torque density remain valid.

## V.    DESIGN EXAMPLE

The FASR design example is now presented, referring to a direct-drive wind turbine alternator of small size (19 kW @ 200 rpm). The ratings are given in Table II. The machine has twelve poles and the rotor has three layers and a regular slot pitch, similar to the one in Fig. 1. The rotor barriers have constant thickness, but their shape is not circular because it is more convenient to move all the barriers towards the airgap, radial-wise, instead. The stator has three slots per pole phase and chorded windings.

The design procedure starts with the maximization of the reluctance torque and hence the rotor anisotropy. The saliency is maximized via a high total insulation and a number of layers equal or higher than three [19-20]. The final design has a saliency ratio of 5, at rated conditions. If the stator leakage inductance components (slot, zig-zag, end windings) were negligible, the saliency ratio would be 8. If also cross saturation and structural ribs were negligible, then the theoretical saliency ratio of the design example would be 13. This to address which factors are affecting negatively the saliency. The thickness of structural ribs depends on the angular speed and the machine size [23], and the slot leakage inductance must be negotiated with the Joule loss density, because longer teeth lower the loss density (31-32), but they also increase the slot and end-winding inductances. The example design has $l_t$ = 22 mm and a split ratio (rotor/stator diameter) equal to 0.8.

Given the airgap and the rotor diameter, closely related to the torque size, the number of poles must be chosen to

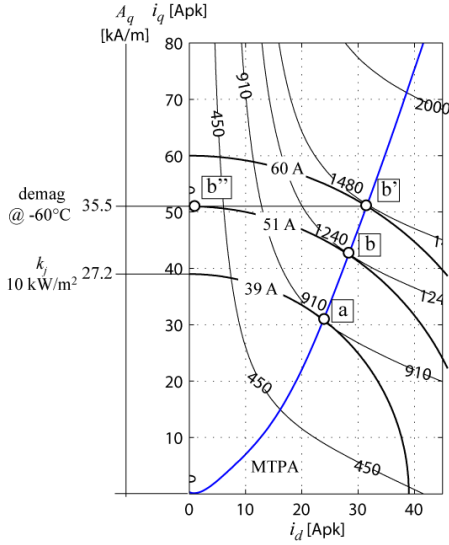produce a pole pitch to airgap ratio *a/g* as high as possible.



Fig. 8     Torque and Ampere contour lines for the machine example described in Table II. The MTPA trajectory is FEA calculated at 130°C.

In this case *g* is 0.75 mm and it is not negotiable. The rotor diameter is 304.5 mm and *a/g* is 106 having chosen *p* = 6. The per-unit insulation is 0.375, a tradeoff between air and iron for the flux guides. The ferrite grade is the one documented in Fig. 4. The cooling setup corresponds to a continuous specific loss $k_j$ = 10000 W/m² (forced ventilation).

## A.     Rated load and overload conditions

The charts of Fig. 8 report the torque and current amplitude contours over the $i_d$, $i_q$ plane of the machine example. They have been FEA calculated at the rated temperature of 130°C. The maximum torque per Ampere (MTPA) control trajectory is also reported.

The continuous electric loading (32) is 27.2 kA/mm, indicated with a red circle in Fig. 7 and on the Aq scale of Fig. 8. The working point at continuous torque is then point *a* having the same electric loading but on the MTPA.

The irreversible demagnetization limit (30), calculated at -60°C, is 35.5 kA/m and it is reported in Fig. 8 (points *b''* and *b'*). Point *b''* is the *q*-current only condition as represented by the magnetic equivalent circuit model. Point *b'* has also the *d*-axis current component but behaves the same as *b''* in terms of demagnetization, at least according to the model. The FEA comparison of two situations of this kind is given in Figs. 9 and 10 and commented later in this section.

Following the conservative approach of Fig. 7 and Table I, the maximum overload condition at -60°C is defined with margin to be point *b* instead of *b'*, as also reported in Table II. With respect to the continuous operating point *a*, point *b* is +30% current and +36% torque (Tables I and II), meaning that even in the hyper worst case situation of -60°C ambient temperature and a cold startup there is still room for transient overload. As the temperature reaches values above the zero the demagnetization exits the area represented in Fig. 8. For example, the current loading limit at 20°C reported in Tables I and II (65.2 kA/m), and the corresponding current (95 A) and torque (2330 Nm) values are out of the range of Fig. 8.

TABLE II – MAIN DATA OF THE EXAMPLE MOTOR

| Mechanical data | | |
|---|---|---|
| Active length (*l*) | 280 | mm |
| Airgap (*g*) | 0.75 | mm |
| Stator diameter (*D*) | 380 | mm |
| Rotor diameter (2*r*) | 304.5 | mm |
| Pole pairs (*p*) | 6 | |
| Pole pitch to airgap ratio (*a/g*) | 106 | |
| Tooth length (*l*ₜ) | 22 | mm |
| **Continuous ratings (point a in Fig. 8)** | | |
| Nominal Speed | 200 | rpm |
| Continuous Torque | 910 | Nm |
| Specific loss ($k_j$) | 10000 | W/m² |
| Electric loading, from eq. (32) | 27.2 | kA/m |
| Current amplitude | 39 | A |
| Phase angle (MTPA) | 53° | |
| **Overload @ -60°C, with margin (point b)** | | |
| Electric loading from Eq. (30) @ -60°C | 35.5 | kA/m |
| Current amplitude | 51 | A |
| Phase angle (MTPA) | 56° | |
| Overload torque @ -60°C | 1240 | Nm |
| **Overload at +20°C, with margin (out of bounds)** | | |
| Electric loading from Eq. (30) @ +20°C | 65.2 | kA/m |
| Current amplitude | 95 | A |
| Phase angle (MTPA) | 63° | |
| Overload torque @ +20°C | 2330 | Nm |
| **Characteristic current** | | |
| @ -60°C | 82 | A |
| | 56.8 | kA/m |
| @ 130°C | 50 | A |
| | 35 | kA/m |

Fig. 9 reports the finite-element PM verification of this latter condition: 65.2 kA/m (95 A) of electric loading on the MTPA and magnets at 20°C in Fig. 9a, same current on the *q*-axis (85 A) without the *d*-axis current in Fig. 9b. This means again a safety margin with respect to the model calculated demagnetization (30): the electric loading on the *q*-axis is 58.3 kA/m instead of 65.2 kA/m. At 20°C the PMs are safe if above 0.10 T.

In Fig. 9b the flux density is homogeneous over the width of all the PMs and nearly the same for all the layers. Also in Fig. 9a, although the overload *d*-axis current saturates the rotor iron, the flux density in the PMs is still fairly uniform, with the exception of the area that is closer to the tips of the barriers. The tips area is represented more in detail in Fig. 10. The flux lines in the tips in Fig. 10a do not follow the direction of magnetization of the ferrite, due to the deep saturation of the rotor flux guides. Flux density values around 2 T are reported in points A and B. Steel saturation and the effect of the *d*-axis current are not considered by the magnetic equivalent circuit model. When only the *q*-current is present (Fig. 10b), the magnets work uniformly as
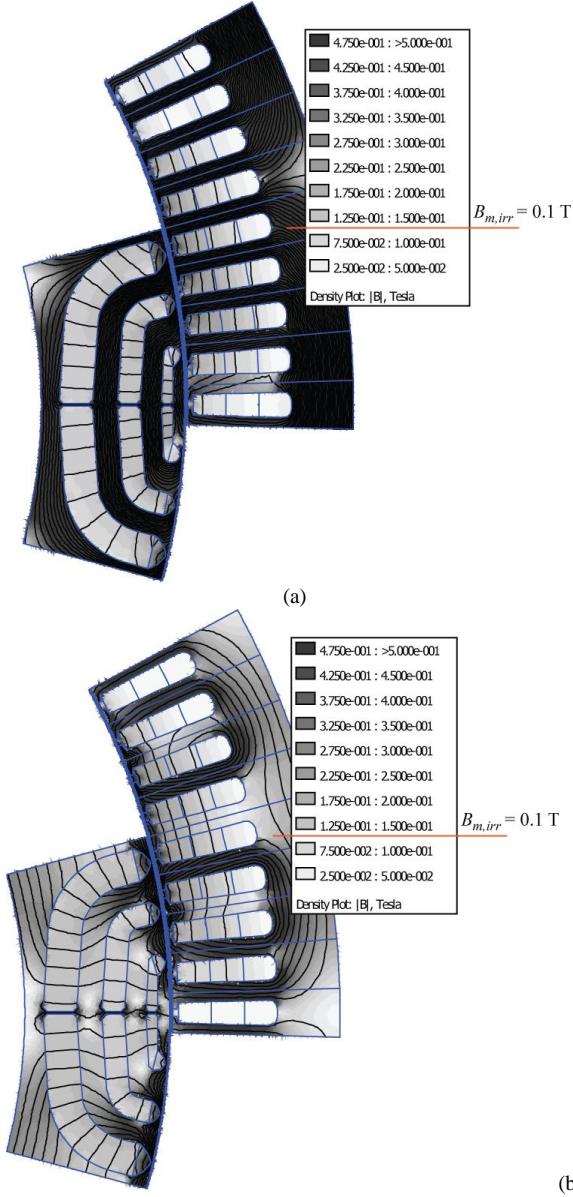
expected.



(a)



(b)

Fig. 9  Flux density maps at maximum overload at 20°C($A_{q,irr}$ = 65.2 kA/m, $B_r$ = 0.38 T, $B_{m,irr}$ = 0.10 T). a) a total loading equal to $A_{q,irr}$ is applied along the MTPA angle ($i_d$ = 43 A, $i_q$ = 85 A) b) same situation, without the $d$ current ($i_d$ = 0, $i_q$ = 85 A), meaning a loading of 0.89 $A_{q,irr}$.

The barriers tips have not been magnetized, as it is intended that they would not be in reality. Even when plastic bonded ferrites are used and they fill the barriers completely, and even if the tips were initially magnetized along the rest of the magnets, they would tend to de-magnetize very easily [9,11]. In most of practical cases the tips are either empty or magnetized poorly.

*B. Steady-state short circuit condition*

Although the current load capability of the machine is not seriously limited by de-magnetization in operation, even at -60°C, a particular care must be given to the short circuit condition. The steady state short circuit current (characteristic current) is aligned against the PMs (then it is along the $q$ axis) and it is maximum at cold, due to the higher remanence of the magnets at low temperature. In the unlikely event of a short circuit fault during a start of operation at cold temperature, the risk of demagnetization is more severe than when in operation, at least for this design example.
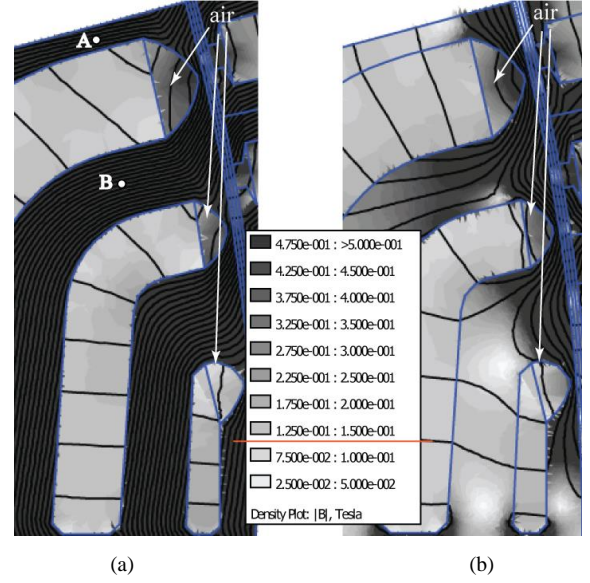


(a)                              (b)

Fig. 10  Enlarged view of Figs. 9a and 9b. The flux density in point A is 2.06 T, and in point B is 2.00 T.

Fig. 11 reports the steady-state short circuit current of the machine of Table II as a function of the PM temperature in the range -60°C to 130°C. The comparison with the irreversible demagnetization limit (30) shows that below -20°C the machine is at risk, in case of fault. Figs. 12 and 13 show the flux density maps in short circuit, respectively at -20°C and +20°C. In both cases the flux density is uniformly distributed in the PMs and it is around 0.2 T. However, $B_{m,irr}$ at -20°C is around 0.2 T and the PMs are then on the edge of irreversible demagnetization in Fig. 12, while at +20°C they are in the safe area, over 0.1 T, in this case.
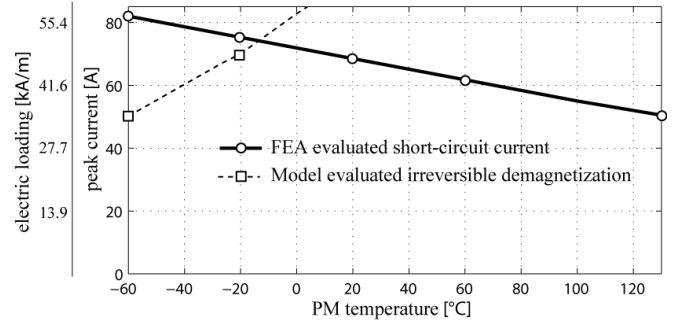


Fig. 11  Crossover temperature between short circuit current and irreversible demagnetization limit

The transient magnetic behavior, in case of a short circuit fault, can worsen the figures presented in this steady state analysis. During the fault transient, in particular if the starting current is much higher than the steady-state short-circuit current, the transient $q$-current loading can be very high and also the eddy current arising in the magnets must be considered as a cause of distortion of the uniform flux density distribution in the PMs. This is demonstrated in [24] for a single layer interior PM machine. A dedicated analysis would be needed to account for transient behavior.

Still, the FEA results demonstrate that the machine example is safe at rated load at all temperatures, and that even at -60°C it can withstand a current overload of +44%. At rated temperature there is no practical limitation, and the margin is so big that all transient effects are also included.

The short-circuit condition suggests to pre-heat the machine to at least zero degrees, before starting non-zero speed operation. Again, transient short-circuit can require a margin with respect to Fig. 11, but it remains true that once the machine is at its steady state operating temperatures there is no danger at all. Last, ferrite grades with higher coercivity values at low temperatures exist [25], and those can be adopted for applications where low operating temperatures are critical.
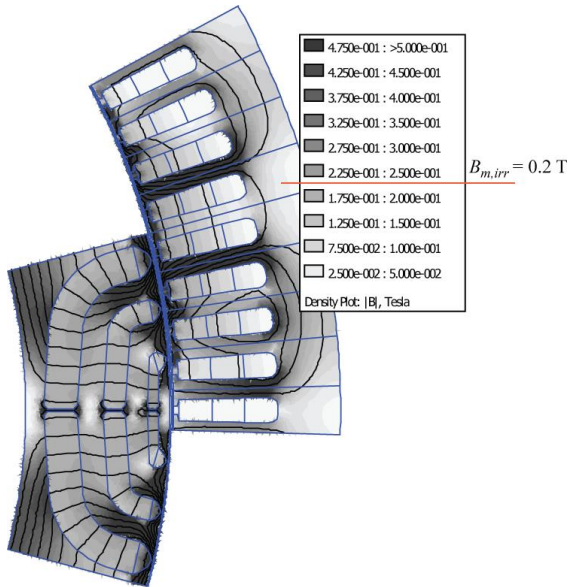


Fig. 12    Steady-state short circuit at -20°C. $B_r$ = 0.42 T, $I_{sc}$ = $I_q$ = 75.25 A.
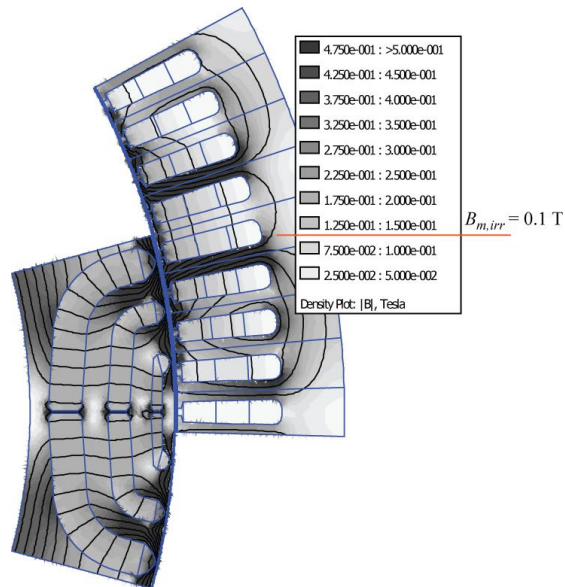


Fig. 13    Steady-state short circuit at +20°C. $B_r$ = 0.38 T, $I_{sc}$ = $I_q$ = 68.5 A.

VI.    CONCLUSION

The paper formalizes a set of the design choices capable of improving the robustness against de-magnetization of a ferrite-assisted synchronous reluctance machine. The design criteria are justified analytically and lead to the uniform exploitation of the low energy density magnetic material. The limit of safe current loading is quantified analytically and shows, by comparison with the continuous loading limit, that larger machines are more at risk of demagnetization than smaller ones. Very low ambient temperatures and cold starts are considered, as they are major causes of demagnetization. The risks related to a short-circuit event when starting at cold ambient are pointed out, showing to be as serious as the maximum load conditions are. FEA validation confirms that the exploitation of the magnets is correct and that the estimation of the critical current loading is precise enough for being of practical use.

REFERENCES

[1]    Pellegrino, G.; Vagati, A.; Guglielmi, P.; Boazzo, B.; , "Performance Comparison Between Surface-Mounted and Interior PM Motor Drives for Electric Vehicle Application," *Industrial Electronics, IEEE Transactions on* , vol.59, no.2, pp.803-811, Feb. 2012.

[2]    El-Refaie, A.M.; Jahns, T.M., "Comparison of synchronous PM machine types for wide constant-power speed range operation," Industry Applications Conference, 2005. Fourtieth IAS Annual Meeting. Conference Record of the 2005 , vol.2, no., pp. 1015- 1022.

[3]    W. Soong and T. J. E. Miller, "Field weakening performance of brushless synchronous AC motor drives," Proc. IEE—Elect. Power Appl., vol. 141, no. 6, pp. 331–340, Nov. 1994.

[4]    Sekerák, P. ; Hrabovcová, V. ; Pyrhönen, J. ; Kalamen, L. ; Rafajdus, P. ; Onufer, M. ; "Ferrites and Different Winding Types in Permanent Magnet Synchronous Motor", Journal of Electrical Engineering, Vol. 63, Issue 3, Pages 162–170, DOI: 10.2478/v10187-012-0024-8, June 2012

[5]    Chino, S.; Ogasawara, S.; Miura, T.; Chiba, A.; Takemoto, M.; Hoshi, N.; "Fundamental characteristics of a ferrite permanent magnet axial gap motor with segmented rotor structure for the hybrid electric vehicle," Energy Conversion Congress and Exposition (ECCE), 2011 IEEE , vol., no., pp.2805-2811.

[6]    Eriksson, S.; Bernhoff, H.; , "Rotor design for PM generators reflecting the unstable neodymium price," Electrical Machines (ICEM), 2012 XXth International Conference on , vol., no., pp.1419-1423, 2-5 Sept. 2012

[7]    Barcaro, M.; Bianchi, N.; Magnussen, F.; , "Permanent-Magnet Optimization in Permanent-Magnet-Assisted Synchronous Reluctance Motor for a Wide Constant-Power Speed Range," Industrial Electronics, IEEE Transactions on , vol.59, no.6, pp.2495-2502, June 2012

[8]    Guglielmi, P.; Boazzo, B.; Armando, E.; Pellegrino, G.; Vagati, A.; , "Permanent-Magnet Minimization in PM-Assisted Synchronous Reluctance Motors for Wide Speed Range," Industry Applications, IEEE Transactions on , vol.49, no.1, pp.31-41, Jan.-Feb. 2013

[9]    Ooi, S.; Morimoto, S.; Sanada, M.; Inoue, Y.; , "Performance evaluation of a high power density PMASynRM with ferrite magnets," Energy Conversion Congress and Exposition (ECCE), 2011 IEEE , vol., no., pp.4195-4200, 17-22 Sept. 2011

[10]    Armando, E.; Guglielmi, P.; Pastorelli, M.; Pellegrino, G.; Vagati, A., "Performance of IPM-PMASR Motors with Ferrite Injection for Home Appliance Washing Machine," Industry Applications Society Annual Meeting, 2008. IAS '08. IEEE , vol., no., pp.1-6.

[11]    Sanada, M.; Inoue, Y.; Morimoto, S.; "Rotor structure for reducing demagnetization of magnet in a PMASynRM with ferrite permanent magnet and its characteristics," Energy Conversion Congress and Exposition (ECCE), 2011 IEEE , vol., no., pp.4189-4194.

[12]    Hosoi, T.; Watanabe, H.; Shima, K.; Fukami, T.; Hanaoka, R.; Takata, S.; , "Demagnetization Analysis of Additional Permanent Magnets in Salient-Pole Synchronous Machines With Damper Bars Under Sudden Short Circuits," Industrial Electronics, IEEE Transactions on , vol.59, no.6, pp.2448-2456, June 2012

[13]    A. Vagati, M. Pastorelli, G. Francheschini, and S. Petrache, "Design of low-torque-ripple synchronous reluctance motors," Industry Applications, IEEE Transactions on, vol. 34, no. 4, pp. 758 -765, jul/aug 1998.

[14]    Oh, Jae Yoon (Seoul, KR) Jung, Dal Ho (Seoul, KR) "Flux barrier synchronous reluctance motor", United States Patent 6239526, Assignee: LG Electronics, Inc. (KR), 2001.

[15]    Jahns, T.M.; Soong, W.L., "Torque Ripple Reduction in Interior Permanent Magnet Synchronous Machines Using the Principle of Mutual Harmonics Exclusion," Industry Applications Conference, 2007. 42nd IAS Annual Meeting. Conference Record of the 2007 IEEE , vol., no., pp.558-565, 23-27 Sept. 2007

[16]    Moghaddam, R.R.; Magnussen, F.; Sadarangani, C.; , "Theoretical and Experimental Reevaluation of Synchronous Reluctance Machine," Industrial Electronics, IEEE Transactions on , vol.57, no.1, pp.6-13, Jan. 2010

[17] RR Moghaddam, "Rotor for a Synchronous Reluctance Machine", US Patent App. 13/230,543, 2011

[18] Vagati, A.; Franceschini, G.; Marongiu, I.; Troglia, G.P., "Design criteria of high performance synchronous reluctance motors," Industry Applications Society Annual Meeting, 1992., Conference Record of the 1992 IEEE , vol., no., pp.66,73 vol.1, 4-9 Oct 1992

[19] A. Vagati and P. Guglielmi et al., "Design, analysis and control of Interior PM synchronous machines". Tutorial Course notes of IEEE Industry Applications Society Annual Meeting (IAS), CLEUP, Padova (Italy), ISBN 88-7178-898-2, pp. 6.1-6.35, 2004.

[20] R.R. Moghaddam, "Synchronous Reluctance Machine (SynRM) in Variable Speed Drives (VSD) Applications". ISBN 978-91-7415-972-1, PhD Doctoral Thesis, edited by KTH, Stockholm, SWEDEN, 2011.

[21] T. Lipo, "Introduction to AC Machine Design", University of Wisconsin Power Electronics Research Center, 1993.

[22] T. J. E. Miller  Brushless PM and Reluctance Motor Drives,  1989 :Clarendon

[23] Barcaro, M.; Meneghetti, G.; Bianchi, N., "Structural analysis of the interior PM rotor considering both static and fatigue loading," Energy Conversion Congress and Exposition (ECCE), 2012 IEEE , vol., no., pp.4338,4345, 15-20 Sept. 2012

[24] J. D. McFarland and T. M. Jahns, "Investigation of the rotor demagnetization characteristics of interior PM synchronous machines during fault conditions," in Energy Conversion Congress and Exposition (ECCE), 2012 IEEE, 2012, pp. 4021-4028.

[25] Hitachi, "High Energy Ferrite Magnets – NMF Series", http://www.hitachi-metals.co.jp/